Evaluation of Hydroxyapatite crystallization in a batch reactor for the valorization of alkaline phosphate concentrates from wastewater treatment plants using calcium chloride

M. Hermassi[a,b], C. Valderrama[a,*], J. Dosta[c], J.L. Cortina[a], N.H. Batis[b]

[a]Chemical Engineering Department. Universitat Politècnica de Catalunya-Barcelona TECH.

[b]Department of Biological and Chemical Engineering, National Institute of Applied Sciences and Technology (INSAT), University of Carthage (Tunisia)

[c]Department of Chemical Engineering, Universitat de Barcelona (UB), Barcelona (Spain)

*Correspondence should be addressed to: César Valderrama

Departament d'Enginyeria Química, Universitat Politècnica de Catalunya

Av. Diagonal 647, 08028, Barcelona Spain

Tel.: 93 4011818, Fax.: 93 401 58 14

Email: cesar.alberto.valderrama@upc.edu

Abstract

In this work, phosphorous recovery as hydroxyapatite ($Ca_5(PO_4)_3OH$(s)=Hap) from alkaline phosphate concentrates (0.25 to 1 g P-PO_4^{3-}/L) using calcium chloride (6 g /L) in a batch reactor was evaluated. Ca(II) solutions was continuously fed (0.1-0.3 mL/min) up to reaching a Ca/P ratio of ~1.67 (5/3) to promote Hap formation. Hap powders were characterized by structural form (using X-ray diffraction (XRD), laser light scattering (LS) and Fourier transform infrared spectroscopy (FTIR)); textural form (using Field Emission Scanning Electron Microscopy with Energy Dispersive System (FE-SEM/EDS) and Brunauer-Emmett-Teller (BET)) and thermally (using Thermogravimetric Analysis (TGA)/Differential Thermal Analysis (DTA)). When pH was kept constant in alkaline values (from 8 to 11.5), Hap precipitation efficiency was improved. At pH 11.5, higher phosphorous precipitation rate was registered compared to that obtained for pH 8 and 10, but lower degree of crystallinity was

observed in the Hap powders. The increase of the total initial phosphate concentration lead to the formation of Hap powders with higher degree of crystallinity and crystal diameter, but also lower mean particle size. As Ca(II) dosing rate increased Hap precipitation rate was higher, and also the mean size and degree of crystallinity of the prepared particles increased.

Keywords: P(V) recovery; Hap precipitation; batch reactor; crystallization; $CaCl_2$; solid characterization.

1. Introduction

Phosphorus management has been recently highlighted by the United Nations Environment Program as one of the main emerging problems to be faced in the next decades. The use of phosphorous needs to become more efficient and its recycling more widespread, since the demand for phosphorus is increasing and the available phosphorous resources are scarce. For instance, the excessive phosphorus content in wastewaters should be removed for controlling eutrophication and maintaining a sustainable environment for future generations. Several physical, biological and chemical processes include adsorption/ ion exchange, chemical precipitation/coagulation, crystallization and membrane filtration/ reverse osmosis for the removal and / or recovery of dissolved phosphates(P(V)) in water and wastewaters have been investigated [1,2,3].

Different research efforts during the last decade, have probed that phosphorus recovery at low levels (e.g. 2-10 mg/L), from domestic and urban waste waters is not economically feasible, using conventional removal processes (coagulation, chemical precipitation, adsorption, ion-exchange) [2,4,5]. However, the introduction of new processes using P-selective sorbents (e.g. metal oxides sorbents or metal oxide impregnated ion exchange resins) will provide concentrated effluents of phosphate (e.g. from 0.1 to 2 g $P\text{-}PO_4^{3-}$/L) typically at alkaline pH values (9 to 12) due to the requirements of the regeneration step using 2 to 5% NaOH

52 solutions [6]. The alkaline P(V)-brines are suitable candidates to recover the phosphate
53 content as (calcium, magnesium, ammonium)–phosphate by-products using Ca(II), Mg(II),
54 NH_4^+ brines generated in many industrial effluents, especially in processes using membrane
55 desalination technologies or using low-cost raw materials [1,7,8].

56 In alkaline solutions, calcium phosphates (Ca-P) are highly stable minerals [9] however
57 involve the crystallization of many metastable precursor phases. Amorphous calcium
58 phosphate (ACP, Ca/P(1.5), $Ca_3(PO_4)_2.nH_2O$), dicalcium phosphate dihydrate (DCPD,
59 Ca/P(1), $CaHPO_4.2H_2O$, brushite), β-whitlockite (β-TCP, Ca/P(1.5), β-$Ca_3(PO_4)_2$) and
60 octacalcium phosphate (OCP, Ca/P(1.33) $Ca_8H_2(PO_4)_6.5H_2O$). All of them are frequently
61 precipitated at low pH values. Hydroxyapatite (Hap) (Ca/P(1.67), $Ca_5(PO_4)_3OH$) is the less
62 soluble phase, preferentially formed in neutral to basic solutions [10,11]. Hap, is a compound
63 with a variable composition existing over Ca/P molar ratios from 1.67 for stoichiometric up to
64 ≈1.5 for fully calcium-deficient Hap [12], and sometimes even outside this range [13]. Direct
65 precipitation of Hap has only been observed for low reactants concentrations, that is, slightly
66 supersaturated or under saturated aqueous solutions with respect to a precursor phase [14,15].
67 Thermodynamically, Hap is postulated to control the PO_4^{3-} concentration in many natural and
68 industrial aqueous streams; however, the remaining P(V) concentration appear to be
69 controlled for lengthy periods by meta-stable phases [9].

70 Hap synthesis by a precipitation route stands out because of its simplicity, low cost, and easy
71 application in industrial production [16,17], although other methods are also used. Different
72 procedures and starting salts have been used as source of phosphate (P(V)) and Ca(II) ions.
73 Boskey and Posner [15], Lagno et al. [10], and more recently Du et al. [18] formed Hap by
74 adding a $CaCl_2$ solution of (pH 7.4-7.6) to a solution of Na_2HPO_4 (pH 10-11), or vice versa at
75 25°C for a Ca/P ratio varied between 1.0 and 1.67.

Koutsoukos et al. [19] also studied the precipitation of Hap at 37°C. Recently, Castro et al. [17] prepared Hap in a batch reactor by neutralization between a saturated $Ca(OH)_2$ solution with orthophosphoric acid solution, using several mixing Ca/P molar ratios (namely, 1, 1.33 and 1.67) at 37°C and a agitation speed of 270 rpm.

Continuous Stirred-Tank Reactor (CSTR), Plug Flow Reactor (PFR) and Batch Reactors (BR) have been set up to study phosphate crystallization. Some researchers have demonstrated that BR have the advantage of providing extreme flexibility of operation and at the same time being physically simple, since all the treatment operations (i.e. flow equalization, precipitation reactions and solids settling) take place in one single tank. Castro et al. [20] also studied the continuous flow precipitation of Hap performed in a meso oscillatory flow reactor at laboratory and pilot-scale at 37°C, at a molar ratio Ca/P of 1.33.

Phosphorous recovery is a topic of great concern nowadays and Hap precipitation has been reported as a suitable process to recover phosphate in a BR, thus, the integration of different technologies (sorption/ion exchange-precipitation) in a waste water treatment scheme can provide an alternative solution for phosphorous recovery. In view of that, the main objective of this work was to assess the recovery of phosphate P(V) from alkaline brines by using Ca(II) solution to precipitate Hap under different experimental conditions in a BR. The alkaline brines were obtained from a P(V) concentration process from waste water using iron-oxide impregnated ion-exchange resins. The Hap precipitation process was evaluated as a function of pH, as well as the Ca(II) dosing rate, the stirring speed and phosphate initial concentration. The Hap precipitates obtained under these operation conditions were properly characterized through the degree of crystallinity, the crystal diameter, the particle size distribution and the thermal analysis.

2. Materials and Methods

2.1 Experimental set-up and procedures

The precipitation of phosphate from aqueous solutions was performed in a two liters lab-scale batch reactor made of glass as can be seen in Figure 1. Agitation in the reactor was provided by a mechanical stirrer (IKA RW 20 and Heidolph RZR) and the stirring speed was ranged from 50 to 250 rpm. pH was monitored in-line by using a pH potentiometer (Crison pH 28). When pH was 0.1 units above or below the set point, strong acid (HCl 1M) or strong base (NaOH 1M) were dosed using a peristaltic pump (Master flex console drive). Experiments batch tests were carried out mixing a volume of NaH_2PO_4 solution (with an initial phosphate concentration between 0.25 to 1.0 g $P-PO_4^{3-}$/L) with a $CaCl_2$ solution (6.0 g Ca(II)/L) added at a flow rate (Q_{Ca}) between 0.1 and 0.3 ml/min (by means of a peristaltic pump Gilson Minipuls 3). The reaction time was ranged between 6 and 24 hours depending on the initial phosphate concentration, the flow rate and in order to reach at the end of the test a molar ratio Ca/P of 1.67, suitable for Hap precipitation. Experiments were performed at room temperature. Three different types of experiments were performed: i) experiments to study the influence of pH (at 8, 10 and 11.5) at constant initial phosphate concentration (1.0 g P-PO_4^{3-}/L), calcium dosing rate (0.1 mL/min) and stirring speed (250 rpm); ii) experiments to study the influence of the total initial phosphate(P(V)) concentration (0.25, 0.375, 0.5 and 1.0 g/L) at constant pH (11.5), calcium dosing rate (0.1 ml/min) and the stirring speed (250 rpm), iii) experiments to study the influence of the stirring speed (50, 100, 150 and 250 rpm) and calcium dosing rate (at 0.1, 0.2 and 0.3 ml/min) at constant pH (11.5) and total initial phosphate concentration (1.0 g P-PO_4^{3-}/L).

Figure 1.

Batch reactor aqueous samples were taken along the experiments and filtered through 0.45 um filter. The total concentrations of the Ca(II) and P(V) were measured by Ion Chromatography

using an Ionex Liquid Chromatography (ICS-1000). The accuracy of the measurements was higher than 95%.

After the conclusion of the experiments, the precipitated solids of the batch reactor were filtered, washed with water several times and dried at T=60°C during 24h. The samples were metalized with gold and then were examined using a JEOL 3400 Field Emission Scanning Electron Microscopy with Energy Dispersive System (FE-SEM-EDS). Samples were also analyzed by Fourier transform infrared spectroscopy (FTIR), in the range 4000cm^{-1}- 500cm^{-1}, (JASCO, FT/IR-4100).

2.1.1 Particle size analysis

Particle size distribution of the Ca-P powder precipitates was analyzed by laser light scattering (LS) with a Coulter diffract particle size analyzer (LS 13 320 Laser Diffraction Particle Size Analyzer Instrument, Beckman Coulter). The size crystal distribution range (CSD) detected was from 0.04 to 2000 μm. The particle size expressed as both volume and number distributions, allows to detect the presence of aggregates and also to assess the size of the majority of the particles, respectively. Particles were analyzed as obtained directly from the batch reactor without any thermal treatment and granulometric separation.

2.1.2 Thermogravimetric Analysis (TGA) and Differential Thermal Analysis (DTA)

Thermogravimetric analyses were carried out in a Mettler TGA/SDTA 851e thermo balance. Dried samples with an approximate mass of 8 mg were degraded between 30 and 800 °C at a heating rate of 10 °C/min in N_2 (100 cm^3/min measured in normal conditions) atmosphere. The precision of reported temperatures was estimated to be ±2 °C.

2.1.3 BET analysis

The specific surface area (S_{BET}) of the powders was measured using multipoint Brunauer-Emmett-Teller (BET) method at low temperature using Micrometrics Flow Sorb II 2300. The equivalent particle diameter (d_{BET}) was calculated from the measured surface area (S_{BET}) values by using Eq. 1 [21].

$$d_{BET} = \frac{6}{\rho S_{BET}} \quad (1)$$

where ρ is the theoretical density of Hap (3.167 g/cm^3).

2.1.4 X-ray diffraction (XRD) analysis

The phase purity and crystallinity of the Hap powder were analyzed by X-ray diffraction with λ CuKα radiation (λ= 1.54056 Å)) at a scanning rate time of 19.2 and 57.6 s, steep angle of 0.015° and 2θ in range of 4-60°. The average crystallite size long c-direction of Hap powder was calculated from (002) reflection in XRD pattern, using Sherrer's equation (Eq. 2) [22]:

$$\tau = \frac{K\lambda}{\beta \cos\theta} \quad (2)$$

where τ (nm) is crystallite size, K is the shape factor (K = 0.9), λ is the wavelength of the X-ray (λ = 0,15406 nm for CuKα radiation), β is the full width at half- maximum (FWHM) (rad) of the peak along (002) direction and θ is the Bragg's diffraction angle.

The crystallinity degree (Xc) was determined using Eq. 3:

$$Xc = (0.24/\beta)^3 . 100\% \quad (3)$$

The solids in powder form were identified by standard Joint Committee en Powder Diffraction Standards (JCPDS) file and it was matched with Powder Diffraction File (PDF) no. 00-009-0432 for Hap.

2.2 Hap precipitation: definition of the experimental conditions

Precipitation processes were designed using the HYDRA-MEDUSA code [23]. Measured P(V) and Ca(II) concentrations were compared when necessary with those predicted by using HYDRA-MEDUSA code. The effect of ionic strength on single salt solubility and formation of pure precipitates was taken into account in the calculations. Aqueous species and mineral phases of the $CaCl_2$-NaH_2PO_4-H_2O system considered on the calculations are detailed in Table 1.

Table 1.

Ca(II) and phosphate ions could forms different Ca-P mineral phases (e.g. $Ca(H_2PO_4)_2$, $Ca_3(PO_4)_2\ (s)$, $Ca_4H(PO_4)_3\ (s)$, $Ca_5(PO_4)_3OH\ (s), CaHPO_4.2H_2O\ (s)$ depending of the aqueous phase composition and the concentrations of the specie involved. The species distribution diagram as a function of pH simulating the conditions of the precipitation assays in three scenarios are shown in Figure 2 a, b and c, respectively: a) excess of P(V) over Ca(II) (molar ratio of 200) simulating the initial step of the precipitation assays; b) an slightly excess of P(V) over Ca(II) (molar ratio of 10) simulating the conditions approaching to the stoichiometric molar ratio, and c) an excess of Ca(II) over P(V) (molar ratio 0.5) simulating the final steps of the precipitation trials. As it can be seen the pH and the levels of concentration of both calcium and phosphate, are influencing the aqueous chemistry and then the precipitation of Ca-P minerals. For a mixture of 10 mM of PO_4^{3-} with 50 µM of Ca^{2+} (Figure 2a) the excess of PO_4^{3--} and $H_2PO_4^-$ ions promotes the formation of complexes as $CaPO_4^-$ and CaH_2PO_4 and it is expected the partial precipitation of $Ca_3(PO_4)_{2(S)}$ above pH 8. The increase of pH above pH 10 favors the formation of the complex $CaPO_4^-$ in solution.

The reduction of the excess of P(V) to Ca(II) for 10 mM of PO_4^{3-} and 1 mM of Ca(II), (Figure 2b) and 20 mM of Ca(II) (Figure 2c), is traduced in the precipitation of ($Ca_5(PO_4)_3OH$(s))

190 from pH values above 6 for a Ca/P ratio of 1.67 and above 5 for solutions with an excess of
191 Ca(II). This is also accompanied by a reduction the $CaH_2PO_4^+$ and $CaHPO_4$ molar fractions.

192 **Figure 2.**

193 **3. Results and Discussion**

194 **3.1 Effect of pH in Hap precipitation**

195 The influence of the pH in the precipitation of P(V) along the experiment for two experiments
196 one at constant pH at 11.5 and other with an initial pH solution at 10.5 (variable pH) as well
197 as the evolution of calcium concentration along the experiment is shown in Figures 3a and 3b.

198 The evolution of pH along the experiment, shown in Figure 3c, follows three differentiate
199 stages. After the initial additions of calcium (up to 0.5 mM Ca(II)) the pH of solution is kept
200 constant between 10.5 to 10.7 taking benefit of the buffer capacity of the initial solution
201 (HPO_4^{-2}/H_2PO_4). The evolution of the total P(V) concentration shows an strong reduction
202 (30% of the initial concentration) as a function of the addition of Ca(II) (3.6 mmol/L) and
203 then it is stabilized around after 240 min, corresponding to the addition of 5.4 mmol/l of
204 Ca(II). As it is shown in Figure 2a the predominant P(V) species in solution between pH 10
205 and 12 is $CaPO_4^-$. Under this conditions it has been postulated a shift on the surface charge of
206 the mineral leading to the precipitation of amorphous calcium phosphate [24], $Ca_3(PO_4)_2$ or
207 β-whitlockite ($\beta - Ca_3(PO_4)_2$) [25] as it is described by Eq. 4.

208 $$3\,CaPO_4^- + H^+ \rightarrow Ca_3(PO_4)_{2\,(s)} + HPO_4^{2-} \qquad (4)$$

209 **Figure 3.**

210 Although potentially such phase can be formed it was not detected at the end of the
211 precipitation test and only Hap, was detected by XRD analysis.

The addition of Ca(II) is traduced into slightly decrease of P(V) concentration as it is observed in Figure 2b, and an increase of the total Ca(II) concentration in solution as can be seen in Figure 3a. Subsequently the pH decreased with a S-shape form due to the reduction of the HPO_4^{2-} concentration by formation of Hap (Figure 3c). After this abroad change the pH of the solution diminished slowly as it is reached the $H_2PO_4^- / HPO_4^{2-}$ buffer (pKa2 = 7.2). During this second stage, pH decreased from 10 to 7.4 and phosphate ions P(V) were present in solution mainly as $CaHPO_4$ (see Figure 2a) and the precipitation of Ca-P could be described by reaction Eq. 5.

$$5CaHPO_{4\,(aq)} + H_2O \leftrightarrow Ca_5(PO_4)_3(OH)_{(s)} + 2\,HPO_4^{2-} + 4H^+ \quad (5)$$

The addition of Ca(II) is traduced in a small decrease of pH during the last stage indicating the growing of formed Hap. Although an excess of Ca(II) was added the removal of phosphate from solution only reached a 50%.

On the other hand, in the experiment with constant pH (11.5 ± 0.1) the phosphate profile shows a continuous decrease with the addition of Ca(II) reaching a removal of phosphate higher than 96% (± 2%) (Figure 3a). At the end of the experiment the precipitated solid was identified as Hap as described latter. The levels of total Ca(II) concentration in solution were below of 20 mmol/L. These values were two orders of magnitude higher than those predicted assuming that the system was equilibrated with Hap, which indicates that the system did not reach equilibrium.

The evolution of phosphate ((P(V)) concentration and recovery as a function of calcium concentration at constant pH values (8, 10 and 11.5) are shown in Figure 4.

Figure 4.

It can be seen (Figure 4b) that precipitation /crystallization of Hap can be divided in three well-defined stages for experiments at constant pH of 10 and 11.5 and just two stages for pH 8. In the stage 1 (stage 1), induction period, early nucleation took place and a reduced amount of phosphate was removed during the first 30 min (0.36 mmol Ca(II)/L). The maximum P(V) removal ratios were observed for pH 10 and 11.5 (11 and 6 %, respectively). This initial step in alkaline pH conditions has been described by reaction Eq. 6 [26,17,24]:

$$3Ca^{2+} + 2HPO_4^{2-} \leftrightarrow Ca_3(PO_4)_{2\,(s)} + 2H^+ \qquad (6)$$

Han et al. [24] identified at pH 10, the precipitation of an amorphous calcium phosphate (ACP) phase at the initial reaction time and then it crystallized into Hap after 2h of reaction. In the second stage (stage 2), the homogenous nucleation of Hap occurred (from 30 to 180 min equivalent to 1.8 mmol Ca(II)/L). During the nucleation stage, the total concentration of Ca(II) remained constant to 0.80 ± 0.2 mmol Ca (II)/L and the P(V) removal increased from 2 to 10% for pH 10 and from 5 to 20% for pH 11.5 (Figure 4). In the final stage (stage 3), further homogeneous nucleation bulk precipitation of Hap was observed, until reaching a final P(V) removal efficiency of 81% and 95%, for pH 10 and 11.5, respectively. Analysis at the end of the experiment of solid samples by XRD analysis determined the presence of Hap. Values of Ca(II) concentration measured along the experiments were higher than those predicting equilibrium with the formation of Hap, indicating a kinetic control, however at the end of the experiment under excess of Ca(II) the measured and calculated values were in agreement.

At pH 8, the two stages observed were the precipitation of Hap, with a phosphate removal ratio up to 20%, followed by a homogeneous nucleation stage of Hap with a phosphate removal ratio up to 78%. This is in agreement with results reported in literature at pH 7.5 in which Hap phase was directly observed immediately the reaction was started [26].

3.2 Influence of initial P(V) concentration

The evolution of total P(V) concentration phosphate profiles for experiments carried out at constant pH (11.5±0.2) for initial phosphate concentrations of 0.25, 0.375, 0.5 and 1.0 g P-PO_4^{3-}/L are shown in Figure 5. The total P(V) concentration decreased with the addition of Ca(II) reaching a final concentration below 0.2 mg P-PO_4^{3-}/L (limit of quantification for (P(V)) in this study), which stands for more than 65 % of P(V) removal as Hap as it was determined by XRD analysis. Total Ca(II) concentrations in solutions were below the limit of quantification, for the lower P(V) concentrations and below 1 mmol/L for the concentrated experiment (1.0 g/L), indicating a total phosphate removal (> 99%) as a Hap with a Ca/P ratio of 1.67, approximately.

Figure 5

The kinetics of precipitation of Hap is important in explaining the oversaturation of aqueous phase with respect to initial phosphate and calcium concentration. Consequently, several empirical equations have been used to describe the kinetics of Hap based on driving forces calculated from disequilibrium [19,27]. Inskeep and Silvetooh [28] determined the rate reaction order with respect to solution or surface area and determined that the rate of Hap at pH 7.4 to 8.4 could be expressed by Eq. 7 as follow:

$$R = K_f \,.\gamma\,(\mathrm{Ca}^{2+}).\gamma\,(\mathrm{PO}_4^{3-})\mathrm{S}\,[\mathrm{Ca}^{2+}][\mathrm{PO}_4^{3-}] \qquad (7)$$

where R is the rate of Hap precipitation (mol Hap/ L·s), k_f is the rate constant (L^2 /mol·m^{2}·s), $\gamma\,(\mathrm{Ca}^{2+})$ and, $\gamma\,(\mathrm{PO}_4^{3-})$ are the divalent and trivalent ion activity coefficients, respectively, s is the surface area (m^2 /g), and [Ca^{+2}] and [PO_4^{-3}] are the molar concentrations of Ca^{+2} and PO_4^{-3} (mol/L).

As it could be seen in Figure 5, for each experiment at a given concentration, the Ca(II) concentration was below 0.05 mmol/L (the detection limit in this study) for 0.25 and 0.375 g P- PO_4^{-3}/L; 0.15 mmol/L for 0.5 g P-PO_4^{-3}/L and 0.7 mmol/L for 1.0 g P-PO_4^{-3}/L. Additionally the surface area of the precipitated Hap, in each experiment, ranged from 67 g/m^2 up to 90 g/m^2 as the initial concentration increases. Then, assuming that for each experiment at a given concentration the values of $k_{F,}$ $\gamma(Ca^{+2})$, $\gamma(PO_4^{-3})$, S and $[Ca^{+2}]$ are constant, the precipitation rate equation could be simplified to Eq. 10:

$$R = -\left(\frac{1d[PO_4^{3-}]}{3dt}\right) = k_f.\gamma\,(Ca^{2+}).\gamma\,(PO_4^{3-})S\,[Ca^{2+}][PO_4^{3-}] = k'_f[PO_4^{3-}] \qquad (10)$$

and integrating Eq. 10 between a given t, with [P(V)] and time t=0 for $[P(V)]_0$ it could be obtained:

$$Ln\,\frac{[PO_4^{3-}]}{[PO_4^{3-}]_0} = -k'_f t \qquad (11)$$

where t is time (s), and $k'_f = k_f.\gamma\,(Ca^{2+}).\gamma\,(PO_4^{3-})S\,[Ca^{2+}]$

The evolution of the $Ln\,\frac{[PO_4^{3-}]}{[PO_4^{3-}]_0}$ as a function of time (Figure 6) follows a linear dependence for each [P(V)] concentration. The slopes of these functions were used to calculate the precipitation rate constants k'_f at pH 11.5 (Table 2). The decrease of P(V) concentration from 1.0 to 0.25 P-PO_4^{-3} g/L is traduced in an increase of the k'_f constant up to 2.5 times. It indicates that the rate of Hap precipitation follows the proposed first order rate with respect to Ca^{2+}, PO_4^{3--}, and surface area [28,16].

Table 2.

Figure 6.

3.3 Influence of stirring and Ca(II) addition rate

Phosphate precipitation experiments under different stirring speeds in the range 50 rpm up to 250 rpm were carried out. The phosphate concentration evolution did not show any significant influence on the P(V) recovery ratio as it can be seen in Figure 7a, and indicating the absence of mass transfer phenomena limitations. The percentage of P(V) recovery was always above 95± 3 %.

On the other hand, the increase of Ca(II) dosing addition up to 0.3 mL/min, was traduced in the increase of the phosphate removal ratio above 99% (Figure 7b) and the phosphate precipitation rate was slightly higher than for lower dossing ratios as was described previously by Xie et al. [29].

Figure 7.

3.4 Precipitate Characterization

The nature of the solids and crystals formed were characterized by XRD (diffraction patterns are shown in Figure 8 and summarized in Tables 3 and 4). A single phase Hap powder is shown in Figure 8, according to the reference Hap (see Table 3), was obtained in the different experiments (e.g. constant and variable pH and also at different initial phosphate concentration). The strongest peak intensity of the Hap samples at $2\Theta = 31.87°$ was of the (211) crystal plan and the other peak at $2\Theta = 25.87°$ corresponds to the (002) crystal plane. Besides, the other characteristic peaks with less intensity were of the (112) and (300) crystal plane.

It is important to point out that 211 and 002 reflection intensities showed an increased trend by increasing solution phosphate concentration as is shown in Figure 8, which indicates that maturation in Hap crystallinity took place with time.

In fact, the degree of crystallinity or the fraction of the crystalline phase X_c for the hydroxyapatites obtained through different initial phosphate concentration can be evaluated by using equation 3.

Figure 8.

Table 3.

Table 4.

Main functional groups of the different powder Hap samples were confirmed by FTIR analysis (data not shown). It was detected the presence of characteristic bands around 600 cm^{-1} corresponding to ν4 (OPO, PO_4^{3-}) bending mode. Also the 960 cm^{-1} band was assigned to ν1 (PO) symmetric stretching and a band in the range 1100-1000 cm^{-1} was assigned to ν3 (PO, PO_4^{3-}) antisymmetric stretching mode. The small band around 875 cm^{-1} can be attributed to the vibrational frequencies of carbonate ions or HPO_4^{2-} group [30]. Furthermore, the carbonate peaks in the range 1500-1400 and 868 cm^{-1}, corresponding to the asymmetric stretching (ν3 mode) and out of plane bending (ν2 mode) vibrations, respectively [31,32,33] were identified. Presence of these bands is characteristic of a carbonate Hap of B-type, where the carbonate ions occupy the phosphate ions sites [30,34]. The formation of carbonate could be due to the adsorption of atmospheric CO_2 during the ripening time, due to the highly alkaline conditions in the solution [31,33,35].

3.5 Characterization of the degree of crystallinity, crystal diameter and particle size distribution

347 The Hap crystal diameters (calculated by Eq. 2) showed that the powders prepared are mostly
348 constituted by nanoparticles as it is summarized in Table 4. The crystal diameter increased
349 with decreasing de pH of the crystallization process, namely from 22 nm (pH 11.5) to around
350 30 nm (pH 8). Moreover, the crystal diameter and the degree of crystallinity were similar for
351 pH values of 10 and 8 and presented the lower values. The experiment at variable pH reported
352 similar nanometric powder sizes and crystallinity than those obtained for constant pH at 11.5.

353 Also, the stirring speed affected the degree of crystallinity, with, 83% at 150 rpm, and ranged
354 between and around 20 to 27 % for 75 and 250 rpm. The increase of the Ca(II) dosing flow-
355 rate (from 0.1 to 0.3 ml/min) revealed an slight increase of both crystal size and crystallinity
356 degree (from 22 to 27 nm, and from 27 to 50 %, respectively).

357 For experiments under different phosphate concentrations, the highest degree of crystallinity
358 (27%) and crystal diameter (22 nm) were obtained when the maximum initial P(V)
359 concentration was used (1.0 g P-PO_4^{3-}/L). These findings can be explained by the process of
360 particle formation, inducing, nucleation, growth and aggregation.

361 **Figure 9.**

362 Additionally, and according to Figure 9, the granulometric analysis of precipitated particles in
363 volume of particles (Figure 9a) revealed the formation of aggregates with an average
364 equivalent diameter around 57 μm for variable pH and from 8.8 to 70 μm for constant pH
365 (11.5 to 8). From the particle size laser analysis in number (Figure 9b), the crystals obtained
366 with Hap precipitation with not constant pH ranged in size from 0.063 to 0.405 μm and have a
367 mean equivalent diameter of 0.112 μm, presenting a narrow size distribution curve, similar to
368 those obtained with constant pH (0.107 μm). From the particle size distribution in number of
369 particles, it is observed that powders prepared were mostly constituted by nanoparticles.

370 This enormous decrease variation of the average diameter in the aggregates and the constant
371 crystal mean size (d_{50}) with an increase at constant pH, it is attributed to some degree of
372 heterogeneous nucleation as well as to an aggregation process in the nanometric scale. This
373 aggregation process reduces the number of small crystals [36]. Results also show that the
374 mean size and the aggregation degree of the precipitated particles increased with increasing of
375 the calcium flowrate dosing. As stated in Table 4, Hap particles with a mean size (d_{50}) of 89
376 nm were obtained at calcium flowrates of 0.1 and 0.2 ml/min. For 0.3 ml/min, d_{50} was 431 nm
377 and in large aggregates of about 587 µm. Therefore, it was observed that as the Ca(II) dosing
378 flow-rate was higher, the aggregation phenomenon was more pronounced. Xie et al. [29]
379 described this behaviour and observed that when Ca(II) is added rapidly, the high local super-
380 saturation will affect the dehydratation process and it will influence ions association and the
381 nucleation behavior. On the other hand, the increased d_{50} number through the increase of the
382 flowrate contributes to a distribution of supersaturation in the reaction environment, thereby
383 leading to uniform distribution of the driving force for the nucleation and growth processes
384 and give rise to a narrow size distribution [37].

385 The influence of the initial phosphate concentration on the mean particle size of Hap
386 nanoparticles is shown in Figure 9(c-d). The results indicate that the mean particle size (d_{50})
387 decreased with the increase of the initial P(V) concentration. The decrease of particle size was
388 494, 332, 92 and 89 nm for 0.25, 0.375, 0.5 and 1.0 g P-PO_4^{3-}/L, respectively. Therefore, for
389 initial P(V) concentrations above 0.5 g P-PO_4^{3-}/L, Hap particles with size around 90 nm were
390 obtained. This it is attributed to the fact that the increase of initial P(V) concentration led to a
391 high supersaturation level, which made nucleation and growth very fast, thereby resulting in
392 the generation of small particles as described previously [37,38]. However, a large amount of
393 Hap primary nuclei were spontaneously formed when the concentration reached a rather high

394 value. In this case, the aggregation of Hap primary nuclei was greatly intensified during the
395 reaction, causing the poly-dispersity of Hap nanoparticles as described by Yang et al. [37].

396 From large scale application point of view, the settling velocity was accounted by using the
397 Stokes law. This law describes the dependency of unhindered terminal particle settling
398 velocities on the basis of their diameters and densities under laminar flow condition.

399 If Hap is stimulated to precipitate, the crystal formed must reach a certain minimum size to
400 enable them to acquire enough downward velocity to naturally settle to the base of a typical
401 clarifier tank for collection. Thus, according to the Stokes law for particle settling, the average
402 settling was determined to be 0.005 m/s, this value was constant for experiments at different
403 stirring speed and also for those at initial phosphate concentration above 500 mg P-PO_4/L.

404 In addition, Table 4 reports the specific surface area (S_{BET}) estimated from the specific area
405 (d_{BET}) methodology. An increase in specific surface area of Hap was observed as pH was
406 increased from 8 to 11.5. Moreover, at constant pH of 11.5, S_{BET} increased with increasing
407 initial P(V) concentration. Thus, the increase of surface area represents an increase of the
408 powder reactivity for crystal growth.

409 The specific surface area obtained for experiment at variable pH (initial pH of 11.5) was in
410 the range of 60 m^2/g, but with at constant pH (initial pH =11.5) was incremented to 90 m^2/g.
411 The stirring speed and calcium dosing rate (at pH 11.5) did not significantly affect the specific
412 surface area.

413 The EDS analysis indicated that the samples were predominantly composed of Ca, P and O,
414 the major elements of Hap powders. The SEM/EDS micrographs of the powders obtained
415 from various initial phosphate concentrations, at variable or constant pH are shown in Figure
416 10. The powders consisted of rod like shape and plate-shaped nanometric sized particles. As it

417 can be seen from the particles morphology, there is a distribution of small particles and large
418 agglomerates (consisting of fine cold welded particles).

419 **Figure 10.**

420 A higher tendency to form aggregates was observed with higher initial phosphate
421 concentration and at constant pH (Figure 10b). More nearly monodisperse plate shaped with a
422 length of about 1µm-100 nm was found for initial phosphate concentration above 0.5 g P-
423 PO_4^{3-}/L. This is in accordance with the results reported by Dirksen and Ring [39] who
424 described the appearance of different growth morphologies with the existence of
425 concentration gradients at the crystal surface, which lead to growth instabilities and the
426 formation of dendrites (Figure 10a and b).

427 Besides, the powders obtained in batch tests with variable and constant pH (at initial
428 phosphate concentration of 1.0 g P-PO_4^{3-}/L) showed a morphology of plate-shaped or rod-
429 shaped (Figure 10b-c) with a size around 100 nm. Powders presented a certain degree of
430 aggregation, which can be justified by the amorphous nature of the particles (degree of
431 crystallinity around 27 and 39 % for constant and variable pH, respectively (Table 4)).

432 **3.6 Thermal characterization**

433 In the thermogram analysis, Hap crystals were characterized by a continuous mass loss
434 throughout the increase of temperature. Hap crystals with low degree of crystallinity (Test
435 number 2) reported three thermal transitions of mass loss in the temperature region (Figure
436 11). The first one is of 8% at 560° C $\geq$ T $\geq T_{room}$ corresponding from physic-sorbed and
437 surface absorbed water molecule. The second mass loss of 2.5% (between 560 and 830 °C)
438 can be attributed firstly to the loss of water present in the lattice structure (the so-called
439 strongly related intra-crystalline water) and secondly to the decomposition of phosphate ions

(300-500 °C) [3] and corresponding to the early stages of crystallization. The third mass loss occurs at temperatures higher than 830 °C, in which Hap will dehydrate partially to form the oxy-hydroxyapatite according to Eq. 12 [40]:

$$Ca_{10}(PO_4)_6OH_{2\,(s)} \rightarrow Ca_{10}(PO_4)_6OH_{2-2x}O_{x\,(s)} + xH_2O_{(g)} \quad (12)$$

The thermogram obtained for Hap samples with high degree Hap crystallinity (Test number 8) presented just two thermal transitions in the temperature region. The first one, from room temperature to 830 °C, corresponds to a weight loss of about 12%. This weight loss could be associated to the formation of Hap in advanced crystallization stages and it can be attributed to the phase transitions within hydroxyapatite crystals as was previously reported by Piccirillo et al. [41]. A further thermal process for temperature up to 830 °C, corresponding to a negligible weight loss is assumed to be the result of gradual dehydroxylation of Hap powder by reaction 12.

Figure 11.

4. Conclusions

In this study Hap powders, mostly constituted by nanoparticles, were obtained in a batch reactor from the treatment of concentrated alkaline P(V) effluents obtained in the regeneration of ion-exchange resins using a Ca(II) solution.

Three stages were identified in the precipitation of phosphate as Hap for pH values ranging from 8 to 11.5: a) induction period, with a small decrease in phosphate concentration, b) homogeneous nucleation, with maintaining or even a little increase of phosphate concentration and c) further homogeneous nucleation, with a constant decrease of phosphate.

A constant pH of 11.5 favored a higher precipitation rate of phosphate to form Hap when compared with rate obtained for pH 8, 10 and also at variable pH. However, the degree of crystallinity was higher for lower pH values assessed in this study (namely, 8 and 10).

Higher initial P(V) concentration lead to the formation of Hap precipitate powders with higher degree of crystallinity and crystal diameter, but also lower mean particle size.

As Ca(II) dosing rate increased, phosphate precipitation rate was higher, also the mean size and degree of crystallinity of the prepared particles were increased. Furthermore, the stirring speed (between 50 and 250 rpm) not reported any significate effect on the phosphate precipitation rate.

Acknowledgments

This study has been supported by the ZERODISCHARGE project (CTQ2011-26799) financed by Ministry of Science and Innovation (MINECO, Spain) and the Catalan government (project ref. 2009SGR905).

5. References

[1] Z. Bradford-Hartke, P. Lant, G. Leslie, Phosphorus recovery from centralised municipal water recycling plants, Chem. Eng. Res. Des. 90 (2012) 78–85. doi:10.1016/j.cherd.2011.08.006.

[2] T. Nur, M.A.H. Johir, P. Loganathan, T. Nguyen, S. Vigneswaran, J. Kandasamy, Phosphate removal from water using an iron oxide impregnated strong base anion exchange resin, J. Ind. Eng. Chem. 20 (2014) 1301–1307. doi:10.1016/j.jiec.2013.07.009.

[3] V. Dhand, K.Y. Rhee, S.-J. Park, The facile and low temperature synthesis of nanophase hydroxyapatite crystals using wet chemistry., Mater. Sci. Eng. C. Mater. Biol. Appl. 36 (2014) 152–9. doi:10.1016/j.msec.2013.11.049.

[4] Y. Liu, X. Sheng, Y. Dong, Y. Ma, Removal of high-concentration phosphate by calcite: Effect of sulfate and pH, Desalination. 289 (2012) 66–71. doi:10.1016/j.desal.2012.01.011.

[5] M. Das Gupta, P. Loganathan, S. Vigneswaran, Adsorptive Removal of Nitrate and Phosphate from Water by a Purolite Ion Exchange Resin and Hydrous Ferric Oxide Columns in Series, Sep. Sci. Technol. 47 (2012) 1785–1792. doi:10.1080/01496395.2012.658487.

[6] S. Sengupta, A. Pandit, Selective removal of phosphorus from wastewater combined with its recovery as a solid-phase fertilizer., Water Res. 45 (2011) 3318–30. doi:10.1016/j.watres.2011.03.044.

[7] A.T.K. Tran, Y. Zhang, D. De Corte, J.-B. Hannes, W. Ye, P. Mondal, et al., P-recovery as calcium phosphate from wastewater using an integrated selectrodialysis/crystallization process, J. Clean. Prod. 77 (2014) 140–151. doi:10.1016/j.jclepro.2014.01.069.

[8] I. Katz, C.G. Dosoretz, Desalination of domestic wastewater effluents: phosphate removal as pretreatment, Desalination. 222 (2008) 230–242. doi:10.1016/j.desal.2007.01.160.

[9] O.A. Diaz, K.R. Reodyit, P.A.M. Jr, Solubility of inorganic phosphorous in stream water as influenced by pH and calcium concentration , 28 (1994) 1755–1763.

[10] F. Lagno, S.D.F. Rocha, L. Katsarou, G.P. Demopoulos, Supersaturation-Controlled Synthesis of Dicalcium Phosphate Dihydrate and Nanocrystalline Calcium-De fi cient Hydroxyapatite, (2012).

[11] D.K. and P.G.K. N. Spanos, A. Patis, Precipitation of calcium phosphate from simulated milk ultrafiltrate solutions, Cryst. Growth Des. 2007. 7 (2007) 25–29.

[12] L. Wang, G.H. Nancollas, Calcium orthophosphates: crystallization and dissolution., Chem. Rev. 108 (2008) 4628–69. doi:10.1021/cr0782574.

[13] J.C. Elliott, Structure and Chemistry of the Apatites and Other Calcium Orthophosphates, 18 (1994).

[14] O.S.L. Bruisma, G.M.Vanrosmalen, M.M.Seckler, Phosphate removal in a fluidized bed -I. Identification of physical processes, Wat.Res. 5 (1996) 1585–1588.

[15] L. Boskey, S. Posner, Formation of Hydroxyapatite at Low Supersaturation, I (1974) 40–45.

[16] C. Liu, Y. Huang, W. Shen, J. Cui, Kinetics of hydroxyapatite precipitation at pH 10 to 11., Biomaterials. 22 (2001) 301–6. http://www.ncbi.nlm.nih.gov/pubmed/19362524.

[17] F. Castro, A. Ferreira, F. Rocha, A. Vicente, J. António Teixeira, Characterization of intermediate stages in the precipitation of hydroxyapatite at 37°C, Chem. Eng. Sci. 77 (2012) 150–156. doi:10.1016/j.ces.2012.01.058.

[18] L.-W. Du, S. Bian, B.-D. Gou, Y. Jiang, J. Huang, Y.-X. Gao, et al., Structure of Clusters and Formation of Amorphous Calcium Phosphate and Hydroxyapatite: From

the Perspective of Coordination Chemistry, Cryst. Growth Des. 13 (2013) 3103–3109. doi:10.1021/cg400498j.

[19] M.B.Tomson. and. P. Koutsoukos, Z.Amjad,et al., Calcium Phosphates. A Constant Composition Study, J. Am. Chem. Soc. (1980) 1553–1557.

[20] F. Castro, F. Rocha, J. Anto, Continuous-Flow Precipitation of Hydroxyapatite at 37 ° C in a Meso Oscillatory Flow Reactor, (2013).

[21] S.K. Ghosh, S.K. Roy, B. Kundu, S. Datta, D. Basu, Synthesis of nano-sized hydroxyapatite powders through solution combustion route under different reaction conditions, Mater. Sci. Eng. B. 176 (2011) 14–21. doi:10.1016/j.mseb.2010.08.006.

[22] T.T.T. Pham, T.P. Nguyen, T.N. Pham, T.P. Vu, D.L. Tran, H. Thai, et al., Impact of physical and chemical parameters on the hydroxyapatite nanopowder synthesized by chemical precipitation method, Adv. Nat. Sci. Nanosci. Nanotechnol. 4 (2013) 035014. doi:10.1088/2043-6262/4/3/035014.

[23] I. Puigdomènech, Inorganic Chemistry Department, Inorganic Chemistry Department, Chemical Equilibrium Software Hydra and Medusa, Stock. Sweden. (2001).

[24] G.S. Han, S. Lee, D.W. Kim, D.H. Kim, J.H. Noh, J.H. Park, et al., A Simple Method To Control Morphology of Hydroxyapatite Nano- and Microcrystals by Altering Phase Transition Route, Cryst. Growth Des. 13 (2013) 3414–3418. doi:10.1021/cg400308a.

[25] J.O.Nriagu. And, P.B. Moore, Phosphate Minerals, Springer-Veriag. (1984).

[26] D.A. Skoog and D.M.West., Fundamental of Analytical Chemistry,, (1976) 3th Edition. Saunders Colleg.

[27] E.C. Moreno, K. Varughese, crystal growth of calcium apatite from dilute solutions degree of supersaturation on initial precipitation rates, 53 (1981) 20–30.

[28] W.P. Inskeep, J.C. Silvertooth, Kinetjcs of hydroxyapatite precipitation at pH 7 . 4 to 8 . 4 *, (1988) 1883–1893.

[29] B. Xie, T.J. Halter, B.M. Borah, G.H. Nancollas, Tracking Amorphous Precursor Formation and Transformation during Induction Stages of Nucleation, Cryst. Growth Des. (2014).

[30] S. Koutsopoulos, Synthesis and characterization of hydroxyapatite crystals: a review study on the analytical methods., J. Biomed. Mater. Res. 62 (2002) 600–12. doi:10.1002/jbm.10280.

[31] A. Paz, D. Guadarrama, M. Lopez, Jesus E. Gonzales, N. Brizuela and J.Aragón, a comparative study of hydroxyapatite nanoparticles synthesized by different routes, Quim. Nov. 35 (2012) 1724–1727.

[32] I. Sporysh, E. Shynkaruk, O. Lysko, A. Shynkaruk, V. Dubok, E. Buzaneva, et al., Biomimetic hydroxyapatite nanocrystals in composites with C60 and Au-DNA

nanoparticles: IR-spectral study, Mater. Sci. Eng. B. 169 (2010) 128–133. doi:10.1016/j.mseb.2009.10.039.

[33] F. Castro, S. Kuhn, K. Jensen, A. Ferreira, F. Rocha, A. Vicente, et al., Process intensification and optimization for hydroxyapatite nanoparticles production, Chem. Eng. Sci. 100 (2013) 352–359. doi:10.1016/j.ces.2013.01.002.

[34] E. Landi, G. Celotti, G. Logroscino, a. Tampieri, Carbonated hydroxyapatite as bone substitute, J. Eur. Ceram. Soc. 23 (2003) 2931–2937. doi:10.1016/S0955-2219(03)00304-2.

[35] F. A. Müller, L. Müller, D. Caillard, E. Conforto, Preferred growth orientation of biomimetic apatite crystals, J. Cryst. Growth. 304 (2007) 464–471. doi:10.1016/j.jcrysgro.2007.03.014.

[36] R. Rodriguez.-Clemente. J. Gomez-Morales, J.Torrent-Burgues, Crystal Size Distribution of Hydroxyapatite Precipitated in a MSMPR Reactor, (2001) 1065–1074.

[37] Q. Yang, J.-X. Wang, L. Shao, Q.-A. Wang, F. Guo, J.-F. Chen, et al., High Throughput Methodology for Continuous Preparation of Hydroxyapatite Nanoparticles in a Microporous Tube-in-Tube Microchannel Reactor, Ind. Eng. Chem. Res. 49 (2010) 140–147. doi:10.1021/ie9005436.

[38] M. Kucher, D. Babic, M. Kind, Precipitation of barium sulfate: Experimental investigation about the influence of supersaturation and free lattice ion ratio on particle formation, Chem. Eng. Process. Process Intensif. 45 (2006) 900–907. doi:10.1016/j.cep.2005.12.006.

[39] J. A. Dirksen, T. A. Ring, Fundamentals of crystallization: Kinetic effects on particle size distributions and morphology, Chem. Eng. Sci. 46 (1991) 2389–2427. doi:10.1016/0009-2509(91)80035-W.

[40] D. Bernache-assollant, A. Ababou, E. Champion, M. Heughebaert, Sintering of calcium phosphate hydroxyapatite $Ca_{10}(PO_4)_6(OH)_2$ I . Calcination and particle growth, 23 (2003) 229–241.

[41] C. Piccirillo, M.F. Silva, R.C. Pullar, I. Braga da Cruz, R. Jorge, M.M.E. Pintado, et al., Extraction and characterisation of apatite- and tricalcium phosphate-based materials from cod fish bones, Mater. Sci. Eng. C. 33 (2013) 103–110. doi:10.1016/j.msec.2012.08.014.

Table

Species/solid formation reaction	log K
$2H^+ + PO_4^{3-} + Ca^{2+} \leftrightarrow CaH_2PO_4^+$	21.0
$H^+ + PO_4^{3-} + Ca^{2+} \leftrightarrow CaH_2PO_4$	15.1
$H_2O + Ca^{2+} \leftrightarrow CaOH^+ + H^+$	-12.8
$PO_4^{3-} + Ca^{2+} \leftrightarrow CaPO_4^-$	6.5
$2H^+ + PO_4^{3-} \leftrightarrow H_2PO_4^-$	19.6
$3H^+ + PO_4^{3-} \leftrightarrow H_3PO_4$	21.7
$H^+ + PO_4^{3-} \leftrightarrow HPO_4^{2-}$	12.4
$4H^+ + 2PO_4^{3-} + Ca^{2+} \leftrightarrow Ca(H_2PO_4)_2$	39.1
$2H_2O + Ca^{2+} \leftrightarrow Ca(OH)_2 + 2H^+$	-22.8
$2PO_4^{3-} + 3Ca^{2+} \leftrightarrow Ca_3(PO_4)_2$	28.9
$H^+ + 3PO_4^{3-} + 4Ca^{2+} \leftrightarrow Ca_4H(PO_4)_3$	46.9
$3PO_4^{3-} + 4Ca^{2+} + H_2O \leftrightarrow Ca_5(PO_4)_3OH + H^+$	40.5
$H^+ + PO_4^{3-} + Ca^{2+} \leftrightarrow CaHPO_4.2H_2O$	19.0
$Ca^{2+} + H_2O \leftrightarrow CaO + 2H^+$	-32.8

Table 1. Formation constants K (in log value) of the main aqueous and mineral phases involved in the system $CaCl_2$-NaH_2PO_4-H_2O from the HYDRA- Medusa data base [23].

$P(V)_i$ (g/L; mol/L)	$[Ca^{2+}]$ (Hydra-Medusa) (mol /L)	Slope rate Ln P(V)-Ln $P(V)_0$ = f(t)	R^2
1.0; 0.0105	0.839	$k'_f = 0.0014$	0.98
0.5; 0.0052	0.894	$k'_f = 0.0016$	0.84
0.375; 0.0039	0.908	$k'_f = 0.0031$	0.96
0.250; 0.0026	0.922	$k'_f = 0.0041$	0.98

Table 2. Initial experimental condition and linear regression parameters of $\ln[P(V)/P(V)_0]$ as a function of time.

Test number	$FWHM_{002}$	hkl (002) *2θ (°)*	hkl (211) *2θ (°)*	hkl (112) *2θ (°)*	hkl (202) *2θ (°)*	hkl (310) *2θ (°)*	hkl (222) *2θ (°)*
1	0.329	26.14	31.86	32.38	34.21	40.06	46.9
2	0.370	26.18	31.87	32.39	34.21	40.06	46.87
3	0 .268	26.13	31.87	32.19	34.16	39.80	47.11
4	0.272	25.89	31.87	32.06	33.94	39.71	46.73
5	0.383	26.13	31.86	32.25	33.84	39.89	46.98
6	0.586	26.10	31.87	32.20	-	39.66	46.95
7	0.667	26.25	31.87	32.43	34.15	38.95	45.77
8	0.255	25.87	31.85	32.20	34.31	39.93	46.90
9	0.401	26.14	30.66	-	34.15	39.61	47.00
10	0.340	25.98	31.92	32.10	33.87	39.70	46.81
11	0.302	25.80	31.86	32.17	-	39.72	46.87
Powder diffraction File 00-009-0432 (Hap reference)	Relative intensities 2θ (°)	40 25.87	100 31.87	60 32.19	25 34.04	20 39.81	30 46.71

(-) No peak present

Table 3. The full-width at half-maximum (FWHM) and Miller Index (hkl) determined from XRD analysis for HAPs samples

Table 4. Physicochemical characterizations of Hap precipitation under different experimentations conditions: XRD patterns, particle size (LS), specific surface area (BET)

Experimental conditions							**XRD**			**LS**		**BET**	
Test number	**pH control**	**pH**	**P (V) mg P-PO_4/L**	**Ca^{2+} addition Q_{Ca}**	**Stirring speed**	**P(V) removal efficiency**	***$FWHM_{002}$**	**Crystal diameter (ε_{hkl})**	**Degree of crystallinity (Xc)**	**Particle size, d_{50} (in volume)**	**Particle size, d_{50} (in number)**	**S_{BET}**	**d_{BET}**
-	-	-	mg/L	mL/min	rpm	%	-	nm	%	µm	µm	m^2/g	nm
1	No	11→5.5	1000	0.1	250	50	0.329	24.8	38.6	56.5	0.11	59.9	31.6
2	Yes	11.5	1000	0.1	250	95	0.370	22.0	27.2	8.7	0.09	88.3	21.5
3	Yes	8	1000	0.1	250	96	0.268	30.4	71.3	69.5	0.08	34.5	31.6
4	Yes	10	1000	0.1	250	93	0.272	29.9	69.2	6.1	0.11	67.7	28.0
5	Yes	11.5	500	0.1	250	>99	0.383	21.3	24.5	429.3	0.09	90.3	21.0
6	Yes	11.5	375	0.1	250	99	0.586	12.2	6.9	21.3	0.33	73.2	25.9
7	Yes	11.5	250	0.1	250	84	0.667	13.9	4.7	86.5	0.49	66.7	28.4
8	Yes	11.5	1000	0.1	150	85.2	0.255	31.9	83.1	729.9	0.35	93.2	20.3
9	Yes	11.5	1000	0.1	50-75	91.3	0.401	20.3	21.3	23.9	0.09	91.8	20.6
10	Yes	11.5	1000	0.2	250	99	0.340	23.9	35.0	8.3	0.09	53.6	35.3
11	Yes	11.5	1000	0.3	250	>99	0.302	27.0	50.2	587.0	0.43	92.9	20.4

* The full-width at half-maximum (FWHM)

Figure Captions:

Figure 1. Experimental set up of the batch reactor for phosphate precipitation with calcium including a $CaCl_2$ dosing pump, mechanical stirrer, the NaOH and HCL dosing pumps and the pH controller. Solids are removed at the bottom part of the reactor.

Figure 2. Species distribution diagram for the system $CaCl_2$-NaH_2PO_4-H_2O using the HYDRA-Medusa data base [23] under different P(V)/Ca(II) molar ratios: a) excess of P(V) over Ca(II) (molar ratio of 200), b) slightly excess of P(V) over Ca(II) (molar ratio of 10) and c) excess of Ca(II) over P(V) (molar ratio 0.5) for a total ionic strength of 0.5 M.

Figure 3. Evolution of a) phosphate and b) calcium concentration with time in Hap precipitation tests at constant pH (11.5) and variable pH; c) phosphate recovery and pH evolution in variable pH experiment in the batch reactor.

Figure 4. a) The recovery and phosphate evolution profile and as a function of calcium concentration at constant pH values of 8, 10 and 11.5 and b) detail of three crystallization stages in the batch reactor.

Figure 5. Influence of the initial phosphate concentration onto the Hap precipitation at pH 11.5 as a function of total calcium concentration in the batch reactor for a) Phosphate concentration and b) calcium concentration.

Figure 6. Evolution of the $\ln[P(V)/(P(V)_0]$ as a function of time for the precipitation experiments at constant pH (11.5) for phosphate initial concentrations between 0.25 up to 1 g/L using a batch reactor.

Figure 7. Influence of a) stirring speed and b) Ca(II) addition rate on phosphate concentration evolution as function of time during phosphate precipitation in a batch reactor.

Figure 8. XRD analysis of the samples obtained in phosphate precipitation experiments for a) precipitation tests at constant and variable pH and b) precipitation tests under different initial phosphate concentration.

Figure 9. Particle size distribution in a) volume and b) number of Hap obtained from phosphate precipitation test at constant and variable pH and c) volume and d) number of Hap obtained from phosphate precipitation test at different initial phosphate concentration.

Figure 10. FE-SEM of Hap samples obtained from phosphate precipitation at constant pH and different initial phosphate concentration a) 0.5 g P-PO_4^{3-}/L, b) 1.0 g P-PO_4^{3-}/L and c) at 1.0 g P-PO_4^{3-}/L and variable pH and d) EDS analysis of samples at 1.0 g P-PO_4^{3-}/L and constant pH.

Figure 11. Thermogravimetric Analysis (TGA) and Differential Thermal Analysis (DTA) of Hap synthesized at different agitation speed reactor for a) experiment 2 (low degree of crystallinity) and b) experiment 8 (high degree of crystallinity).

Figure

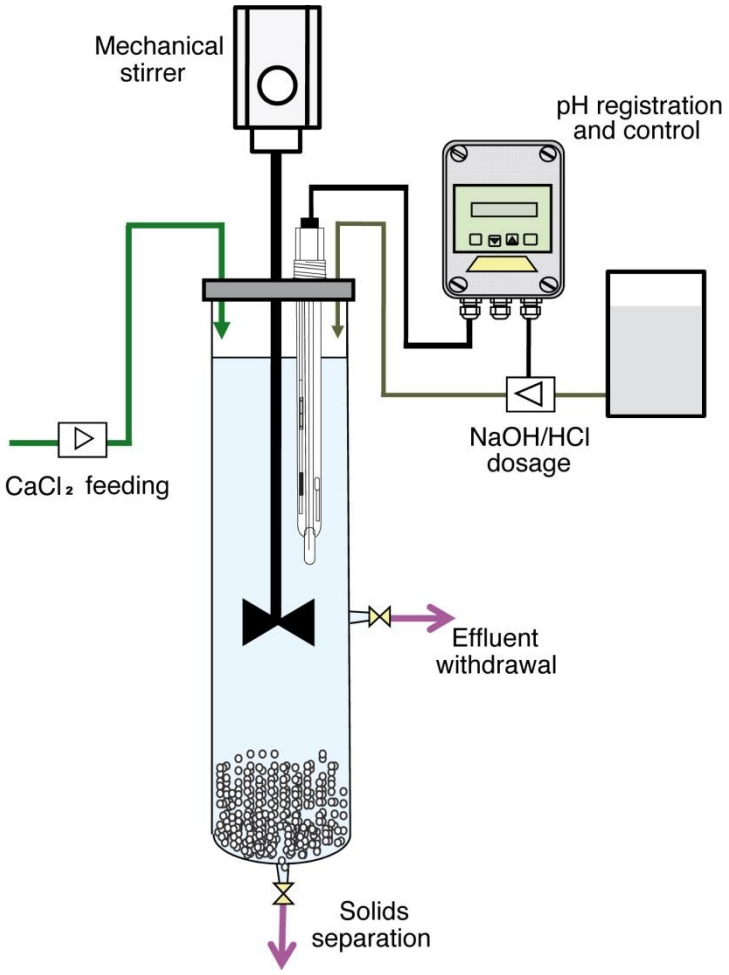

Figure 1.

Figure

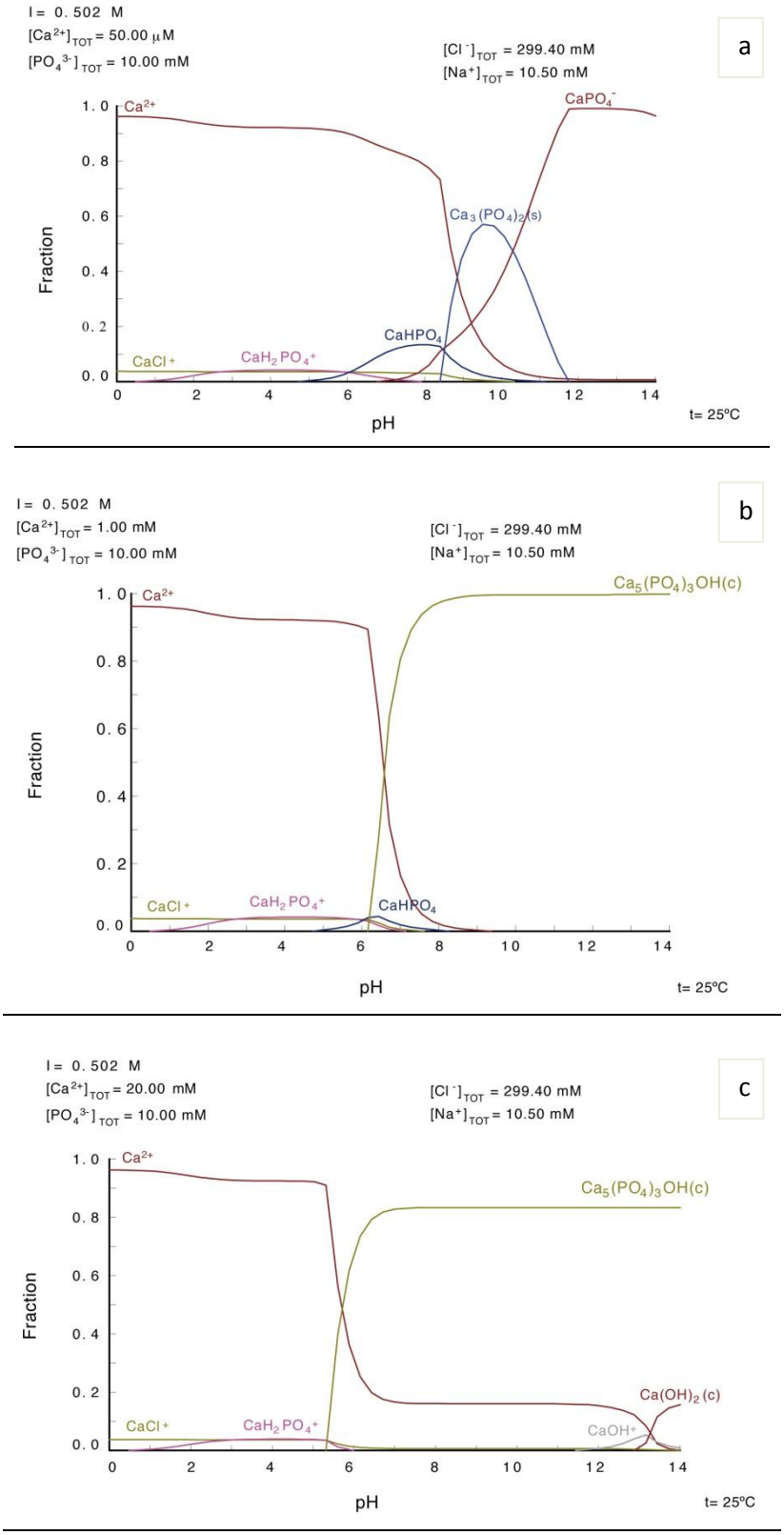

Figure 2.

Figure

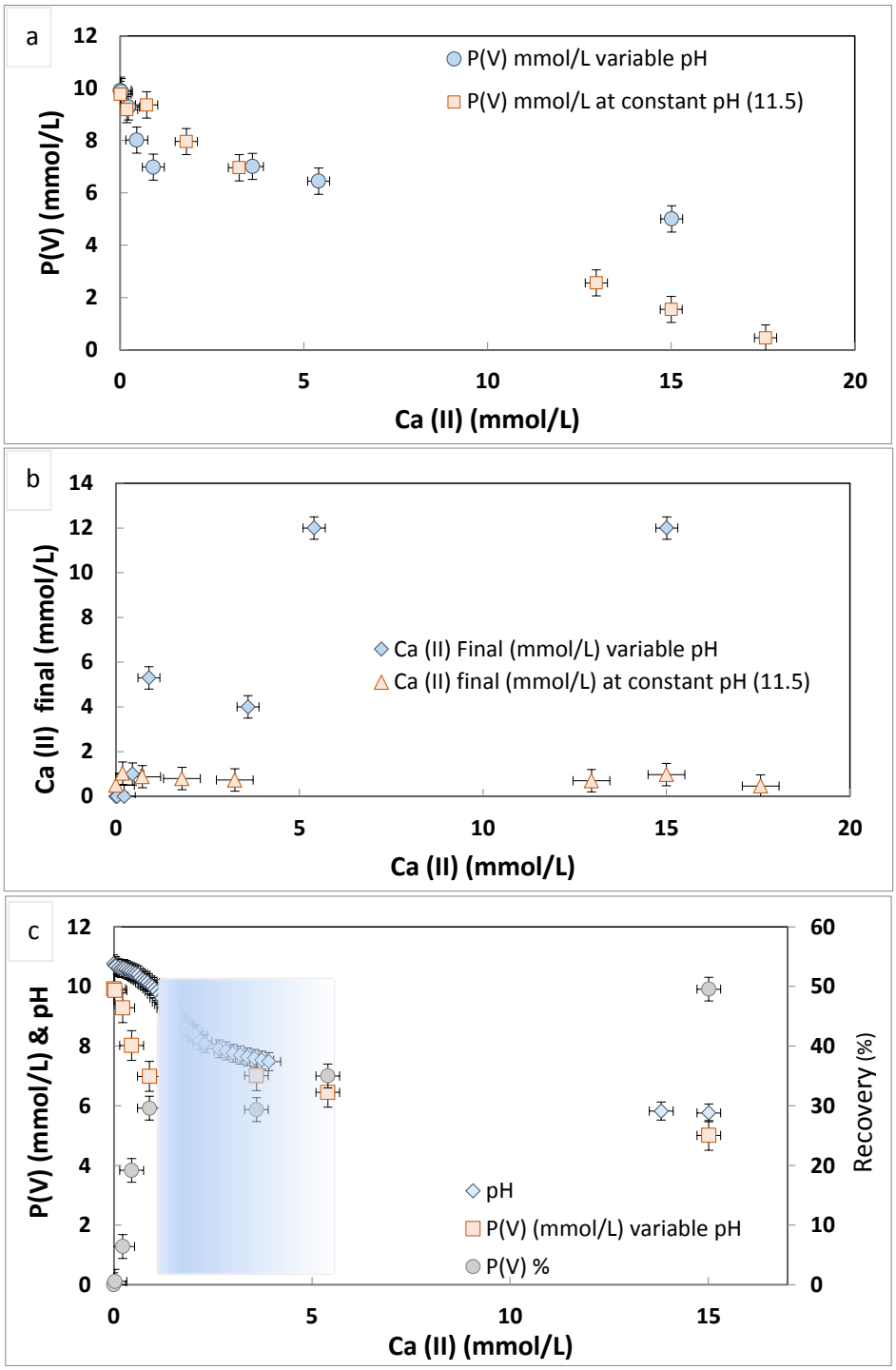

Figure 3.

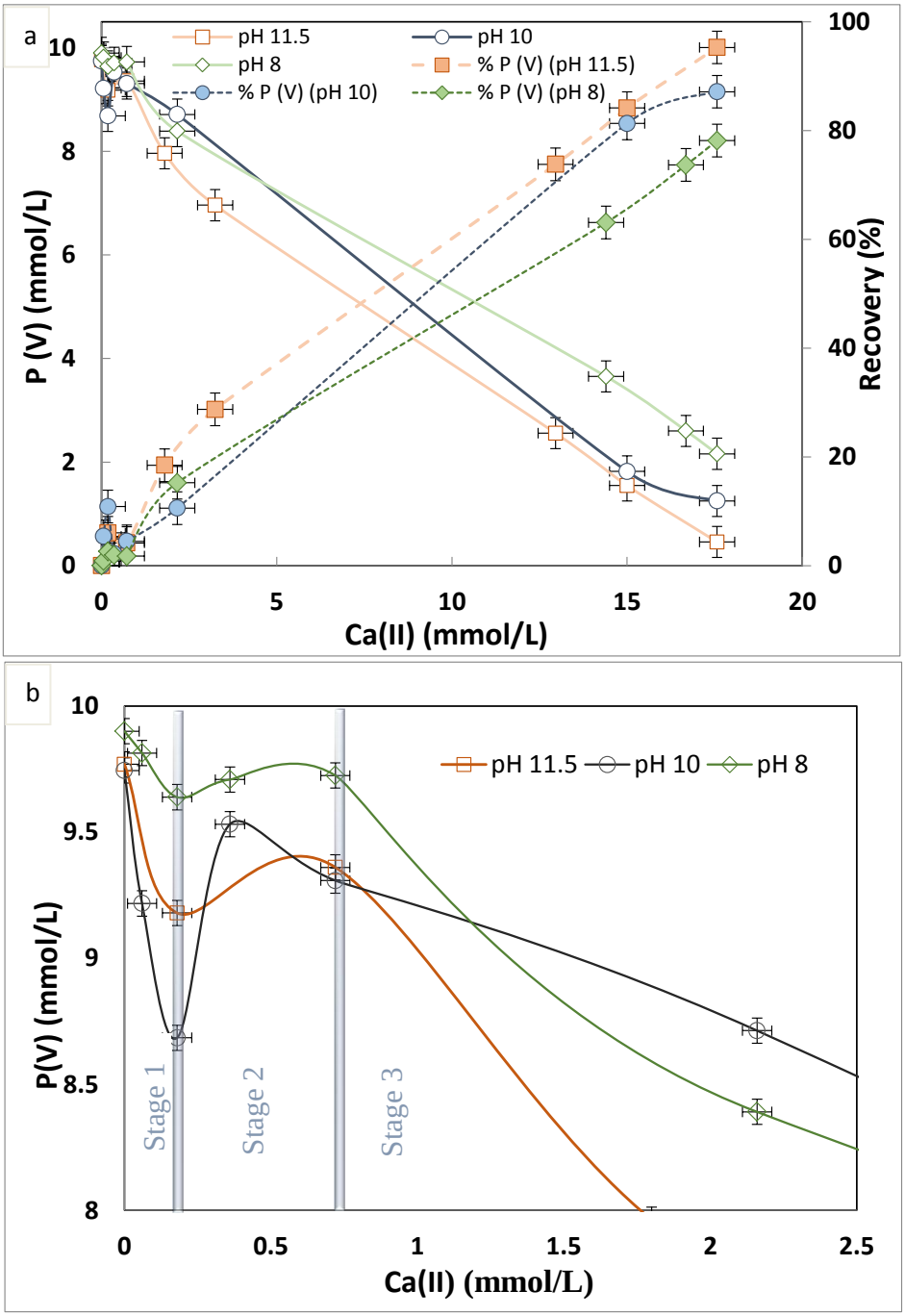
a
pH 11.5
pH 10
pH 8
% P (V) (pH 11.5)
% P (V) (pH 10)
% P (V) (pH 8)
P (V) (mmol/L)
Recovery (%)
Ca(II) (mmol/L)
b
pH 11.5
pH 10
pH 8
P(V) (mmol/L)
Stage 1
Stage 2
Stage 3
Ca(II) (mmol/L)

Figure 4.

Figure

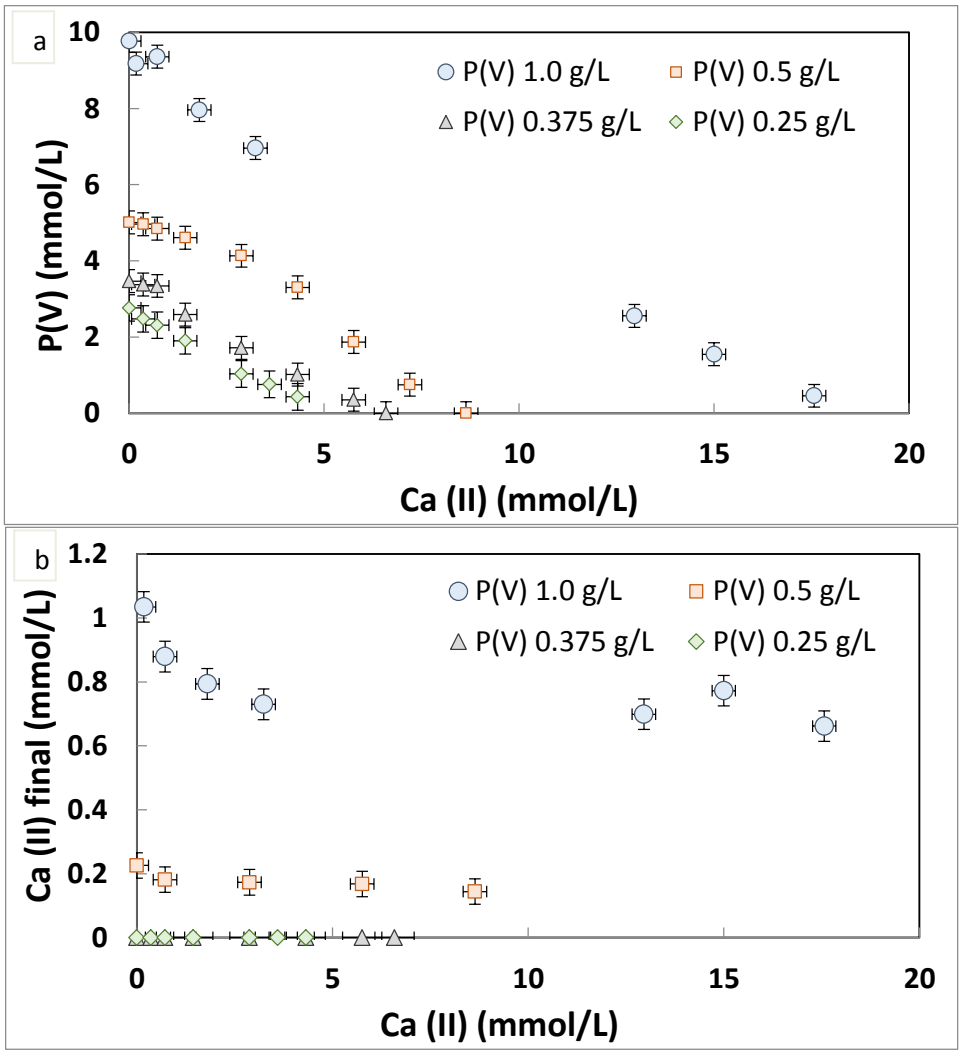

Figure 5.

Figure

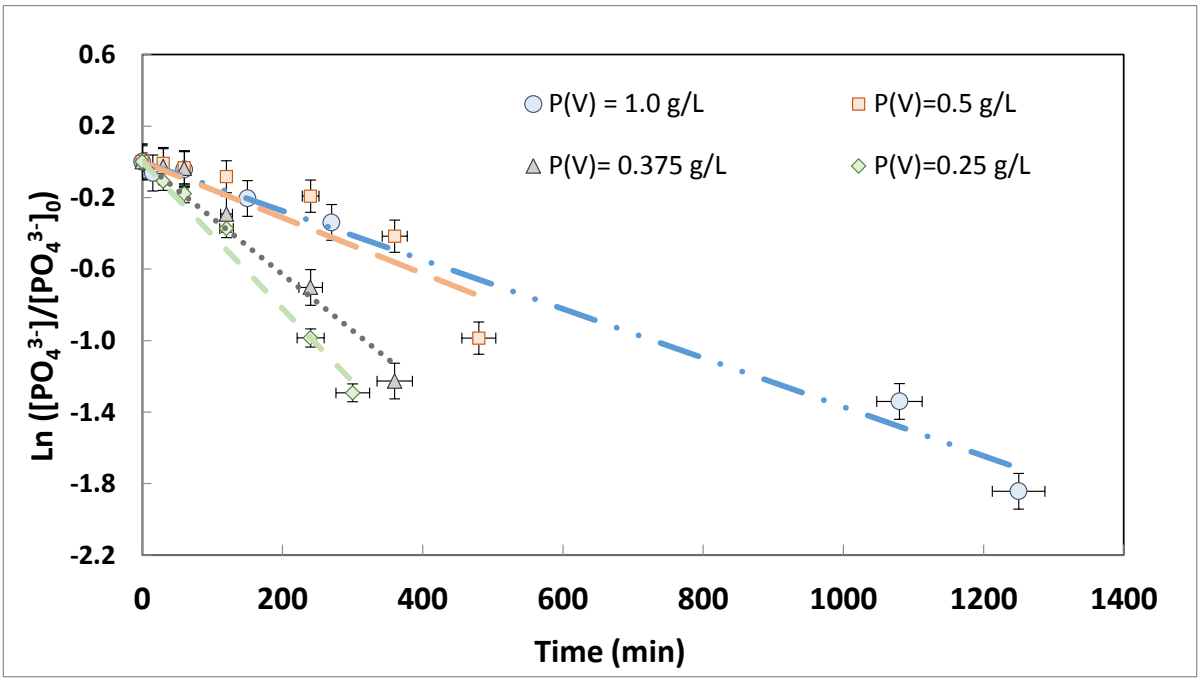

Figure 6.

Figure

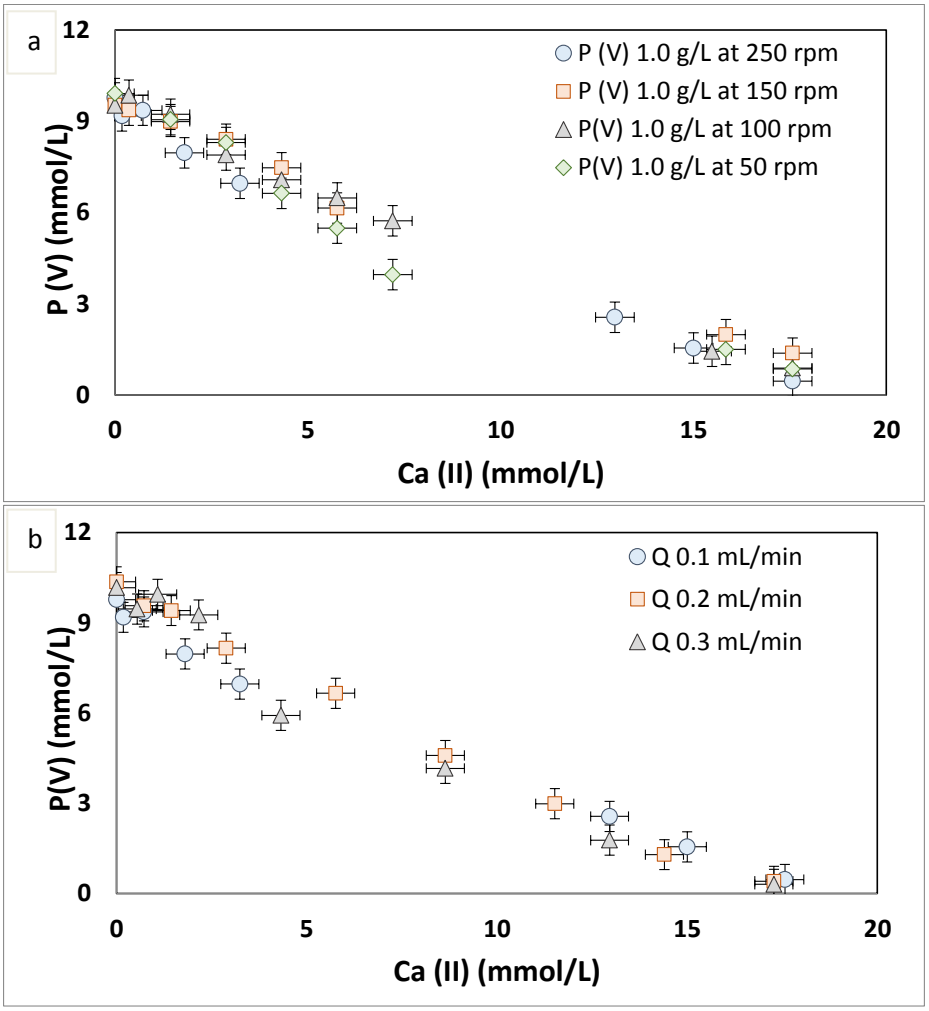

Figure 7.

Figure

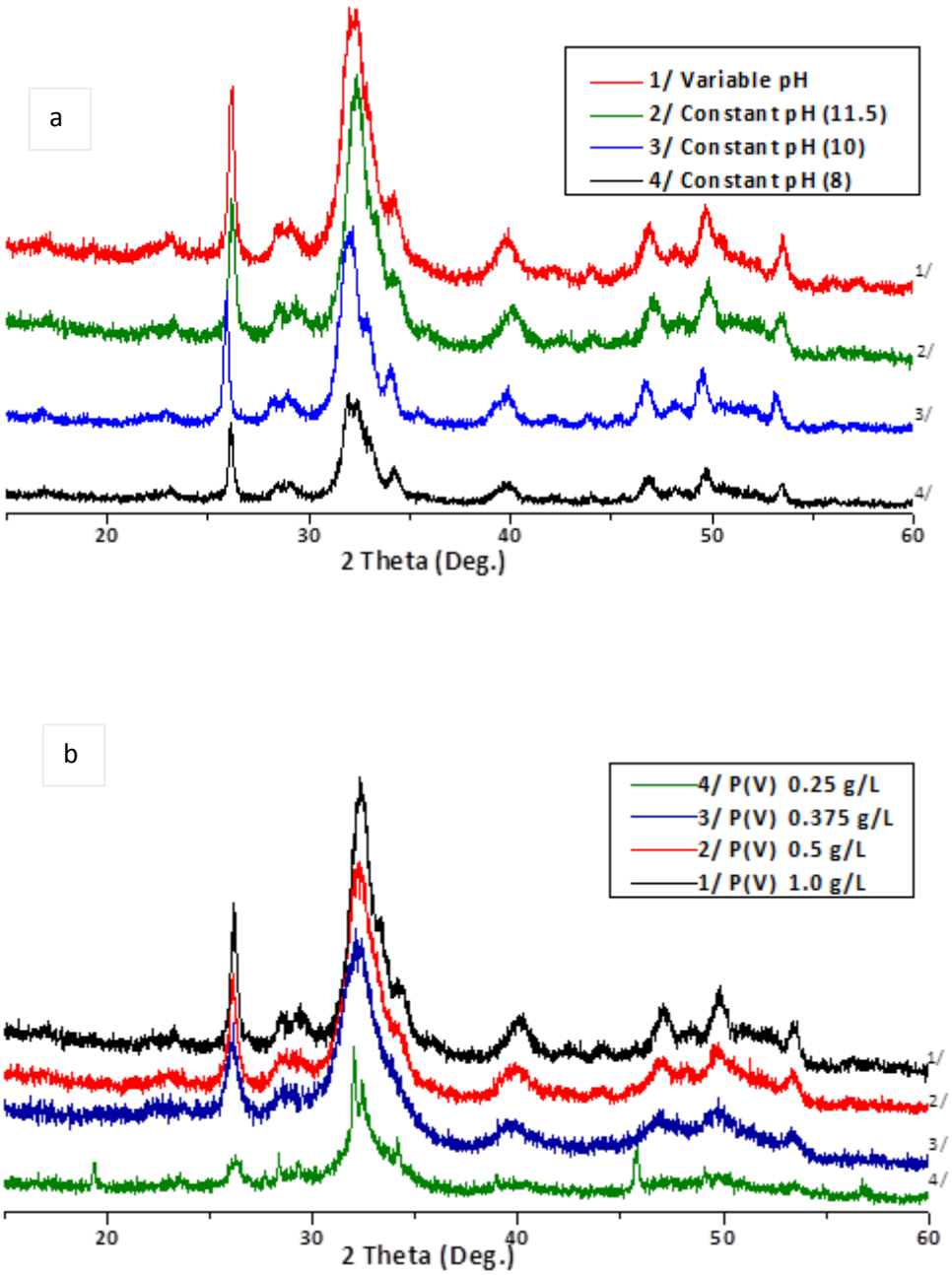

Figure 8.

Figure

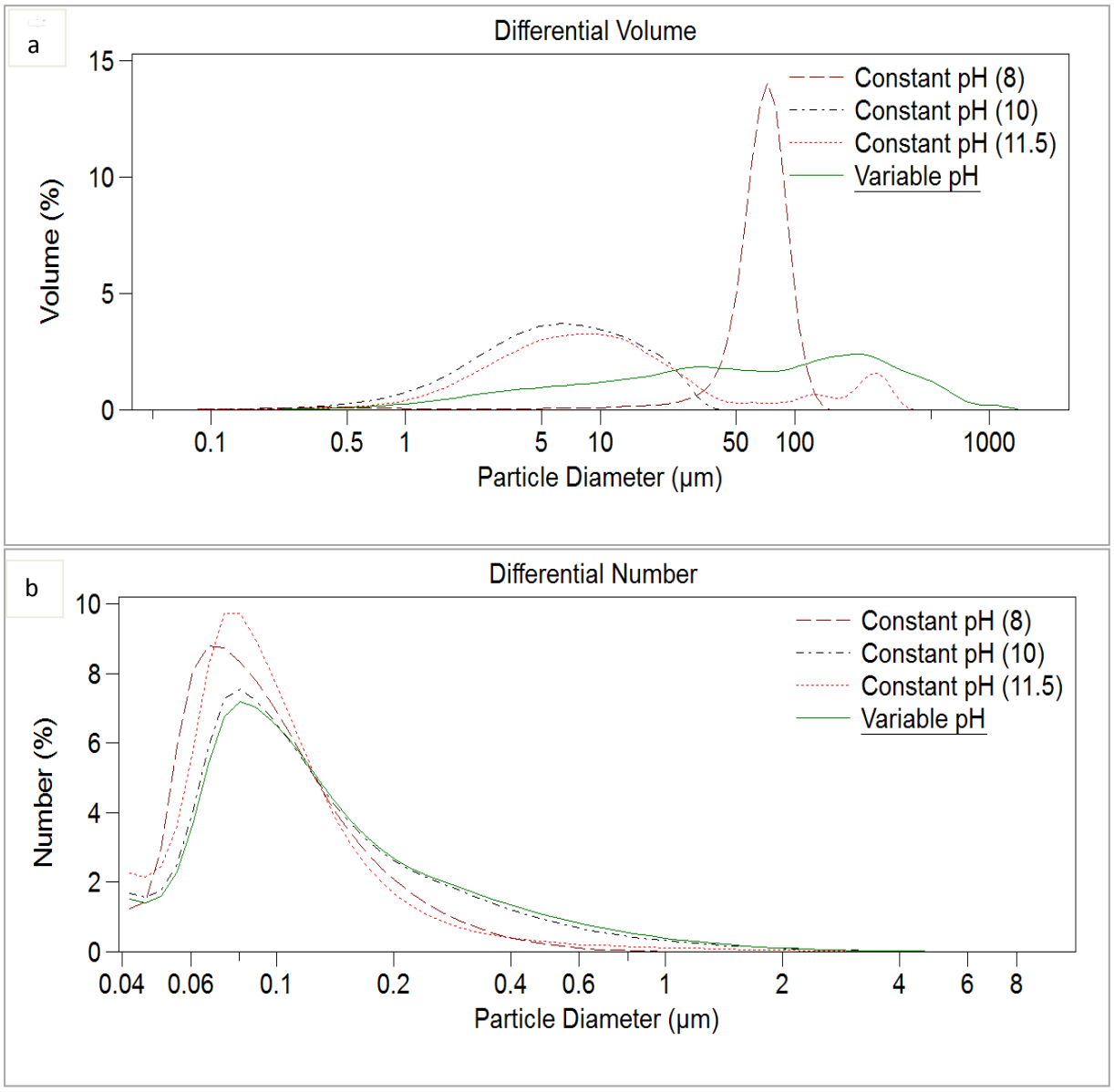
a
Differential Volume
Volume (%)
15
10
5
0
0.1
0.5
1
5
10
50
100
1000
Particle Diameter (µm)
Constant pH (8)
Constant pH (10)
Constant pH (11.5)
Variable pH
b
Differential Number
Number (%)
10
8
6
4
2
0
0.04
0.06
0.1
0.2
0.4
0.6
1
2
4
6
8
Particle Diameter (µm)
Constant pH (8)
Constant pH (10)
Constant pH (11.5)
Variable pH

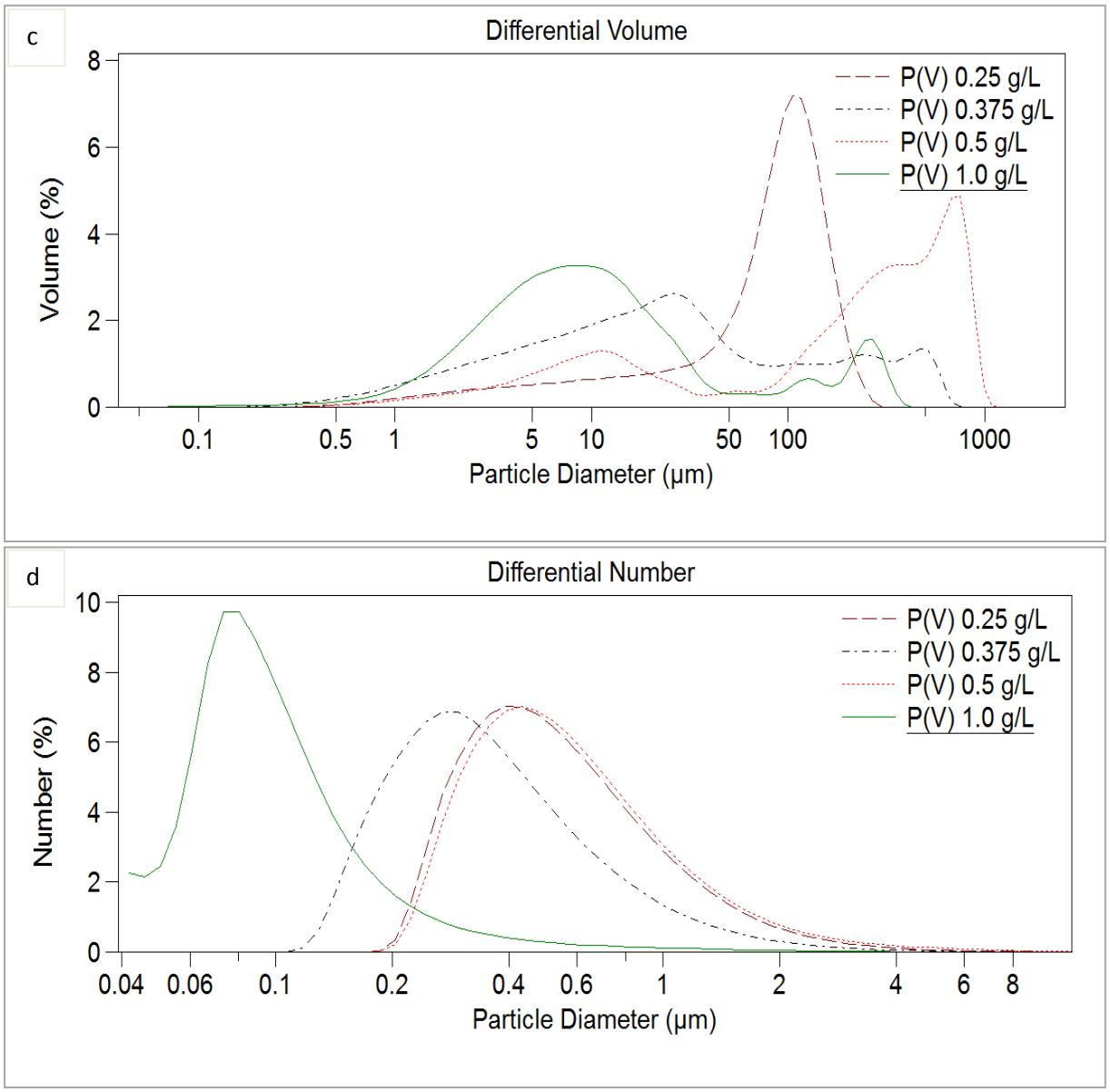
c
Differential Volume
Volume (%)
Particle Diameter (µm)
P(V) 0.25 g/L
P(V) 0.375 g/L
P(V) 0.5 g/L
P(V) 1.0 g/L
d
Differential Number
Number (%)
Particle Diameter (µm)
P(V) 0.25 g/L
P(V) 0.375 g/L
P(V) 0.5 g/L
P(V) 1.0 g/L

Figure 9.

Figure

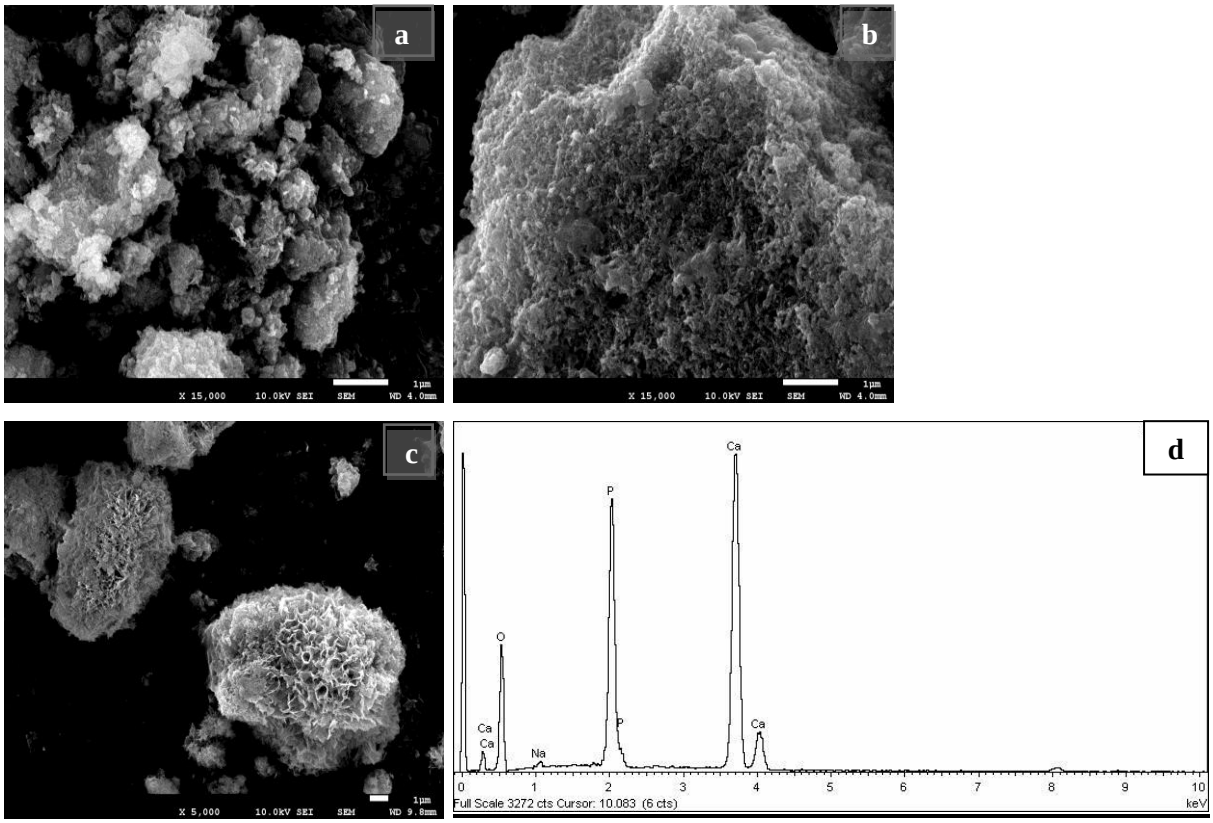

Figure 10.

Figure

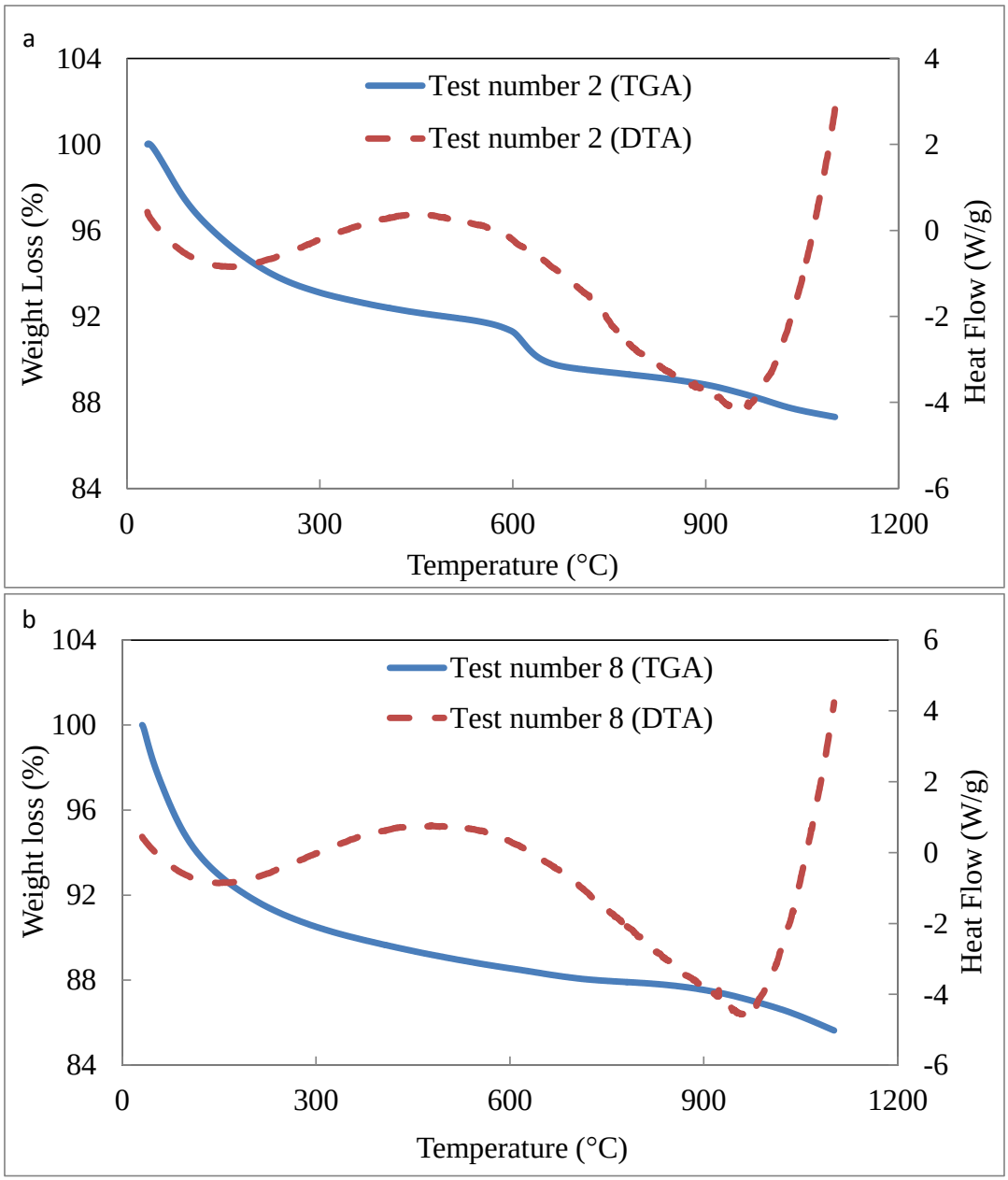

Figure 11.